Supplementary Information (SI) for Journal of Materials Chemistry A.

Supporting Information

Reconstructing a Gd^{3+}-Enriched Inner Helmholtz Plane with Dynamic Electrostatic Shielding Effect for Highly Reversible Zn-Bromine Flow Batteries

Guangyu Zhu[1,2], *Yichan Hu*[2], *Zhenglin Li*[2], *Wei Xiong*[4*], *Haibo Hu*[1*], *Guojin Liang*[2, 3*]

[1]School of Materials Science and Engineering, Anhui University, Hefei 230601, China.

[2]Faculty of Materials Science and Energy Engineering, Shenzhen University of Advanced Technology, Shenzhen, 518055, China.

[3]Institute of Technology for Carbon Neutrality, Shenzhen Institute of Advanced Technology, Chinese Academy of Sciences (CAS), Shenzhen, 518055, China.

[4]Institute of Technology for Future Industry, School of Science and Technology Instrument Application Engineering, Shenzhen Institute of Information Technology, 518172, China.

E-mail: weixiong4-c@my.cityu.edu.hk haibohu@ahu.edu.cn gj.liang@siat.ac.cn

Materials

All chemicals are used as received. Zinc bromide ($ZnBr_2$, ≥98%), potassium chloride (KCl, ≥99%), 1-ethyl-1-methylpyrrolidinium bromide (MEP, ≥99%), and gadolinium nitrate hexahydrate ($Gd(NO_3)_3$, 99%) are obtained from Aladdin. Zn foil (0.2 mm, 99.99%) is purchased from Shengshida Metal Material Co. Ltd. (Dongguan, China). Graphite felt (3.0 mm, carbon ≥99%, bulk density 0.12-0.14 g/cm^2) is received from Yi Reshang. Carbon felt (W0S1011), Carbon cloth, and Carbon paper (HCP010N) are acquired from Shengeru Energy Store. The porous polyolefin membrane is purchased from Wuhan Zhisheng, and the hydrogen tester (BX-168) is obtained from the Aidekesi flagship store.

Preparation of $ZnBr_2$ electrolyte and Gd^{3+}- $ZnBr_2$ electrolyte

Preparation of negolyte: 6.76 g (2 M) $ZnBr_2$, and 2.80 g (2.5 M) KCl are dissolved into 15 mL deionized water to prepare $ZnBr_2$ electrolyte. 2.03 g (0.3 M) $Gd(NO_3)_3$, 6.76 g (2 M) $ZnBr_2$, and 2.80 g (2.5 M) KCl are dissolved into 15 mL deionized water to prepare Gd^{3+}-$ZnBr_2$ electrolyte. Preparation of posolyte: 6.76 g (2 M) $ZnBr_2$, 1.16 g (0.4 M) MEP, and 2.80 g (2.5 M) KCl are dissolved into 15 mL deionized water to prepare a positive electrolyte.

Characterizations

Cyclic voltammetry (CV), linear polarization curves (Tafel), linear sweep voltammetry (LSV), and chronoamperometry (CA) tests are conducted using a conventional three-electrode system in a 2 M $ZnBr_2$ solution, with and without 0.3 M $Gd(NO_3)_3$, at room temperature, using an electrochemical workstation (CHI 760E). The three-electrode system consists of a carbon felt working electrode, a fresh Zn counter electrode, and an Ag/AgCl reference electrode. To analyze the net charge adsorbed on the surface of Zn deposits on the carbon felt in the electrolytes, zeta potential measurements of the Zn anodes are performed. Due to the experimental requirement of dispersing Zn in the electrolyte, commercial Zn powder is used as a substitute for Zn foil. As shown in the test results, the ionic conductivity of the electrolyte is measured using electrochemical impedance spectroscopy (EIS) in symmetric Ti||Ti devices. Activation energies are calculated from the EIS results of symmetric Zn||Zn devices with both electrolytes. The morphologies of Zn deposits on the carbon felt are analyzed using scanning electron microscopy (SEM), and an optical microscope is employed to better illustrate the Zn growth process on different substrates. The crystalline structures of the deposited Zn are characterized using transmission electron microscopy (TEM, JEOL, Model JEMF200) and X-ray diffraction (XRD, Cu Kα radiation, 3°–70°). X-ray photoelectron spectroscopy (XPS, ESCALAB 250Xi) is used to analyze the chemical stability of gadolinium ions in the system. Hydrogen evolution from the Zn negative electrode is tested by measuring the hydrogen volume ratio and pH of the negative electrolyte in the flow battery.

Flow battery tests

To assess long-term stability, a symmetric Zn||Zn flow battery is assembled. Graphite plates serve as current collectors, while carbon felts with a geometric area of 4 cm^2 are used as both the positive and negative electrodes. The positive and negative chambers are separated by a porous olefin membrane. For the electrolyte, a solution of 15 mL containing 0.3 M $Gd(NO_3)_3$, 2 M $ZnBr_2$, and 2.5 M KCl is used for both electrodes. Charge and discharge tests are conducted at room temperature using a LAND multi-channel battery testing system (CT2001A, China). The charging and discharging processes are controlled based on cut-off capacity. In the $ZnBr_2$ full-current battery configuration, the negative electrode is supplied with 15 mL of a solution containing 2 M $ZnBr_2$, 0.3 M $Gd(NO_3)_3$, and 2.5 M KCl, while the positive electrode receives 15 mL of an electrolyte containing a bromine complexing agent. The charging process is controlled by both voltage and capacity, with a safety voltage set to 5 V and a discharge voltage set to 0 V. Peristaltic pumps (BT100-L, Longer, China) circulate the electrolytes into the flow cell at a constant flow rate of 40 mL min^{-1}.

Molecular Dynamics Simulation

The interactions of the Zn atom structures are analyzed using the UFF force field, while Gd^{3+} is modeled with the Merz method. Other interactions are described using the GAFF force field obtained from the AuTo FF web server.

In system 1, the (002) crystal facet structures are fixed on two sides, and 30 Gd $(NO_3)_3$, 200 $ZnBr_2$, 250 KCl, and 5550 H_2O are inserted into the middle of the (002) crystal facet simulation box, which is x = 5.1 nm, y = 5.3 nm, and z =5.8 nm.

In system 2, the (100) crystal facet structures are fixed on two sides, and 30 Gd $(NO_3)_3$, 200 $ZnBr_2$, 250 KCl, and 5550 H_2O are inserted into the middle of the (100) crystal facet simulation box, which is x = 5.1 nm, y = 5.3 nm, and z =5.8nm.

In system 3, the (101) crystal facet structures are fixed on two sides, and 30 Gd $(NO_3)_3$, 200 $ZnBr_2$, 250 KCl, and 5550 H_2O are inserted into the middle of the (101) crystal facet simulation box, which is x = 5.1 nm, y = 5.3 nm, and z =5.8 nm.

The steepest descent method is applied to minimize the initial energy of each system with a force tolerance of 1 kJ·(mol^{-1}·nm^{-1}) and a maximum step size of 0.001 ps before MD calculations. Before

MD simulations, all configurations without Zn facets are annealed from 300 K to 400 K and then back to 300 K in 50 K intervals at each temperature point. A 5 ns simulation is performed under the NPT ensemble at each temperature point. After annealing, the new system is divided into three layers along the Z-axis direction: the upper and lower layers represent the Zn facets, and the middle layer represents the solution. MD simulations are performed using the GROMACS 2021 software package, and the simulations are run for 30 ns. In NVT simulations, the temperature is maintained at 298.15 K using the V-rescale thermostat. The Particle-Mesh-Ewald (PME) method with a fourth-order interpolation is used to evaluate electrostatic interactions, while a cutoff of 1.4 nm is applied to calculate short-range van der Waals interactions.

Reference

1 Van Gunsteren, W. F.; Berendsen, H., A leap-frog algorithm for stochastic dynamics. ***Mol. Simul.*** 1988, 1 (3), 173-185.

2 Spoel D V D, Lindahl E, Hess B, et al. GROMACS: fast, flexible, and free[J]. ***Journal of Computational Chemistry***, 2005, 26(16): 1701-1718.

3 Abraham, et al. GROMACS: high performance molecular simulations through multi-level parallelism from laptops to supercomputers, ***Software X.*** 1-2 (2015) 19–25.

4 H.J.C. Berendsen, D. van der Spoel, R. van Drunen, GROMACS: A message-passing parallel molecular dynamics implementation, Comp. ***Phys. Comm.***, 91 (1995) 43-56.

5 Darden T, York D, Pedersen L. Particle Mesh Ewald: An Nlog (N) Method for Ewald Sums in Large Systems [J]. ***The Journal of Chemical Physics***, 1993,98(12):10089-10092.

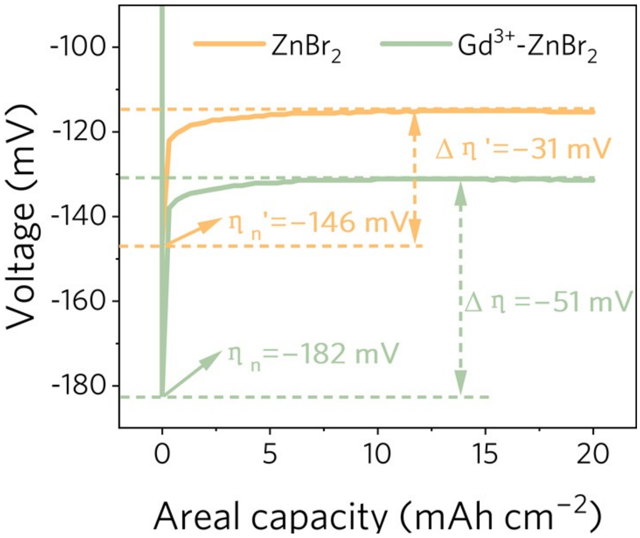

Figure S1. Initial nucleation overpotentials of Zn||Zn flow batteries with different electrolytes.

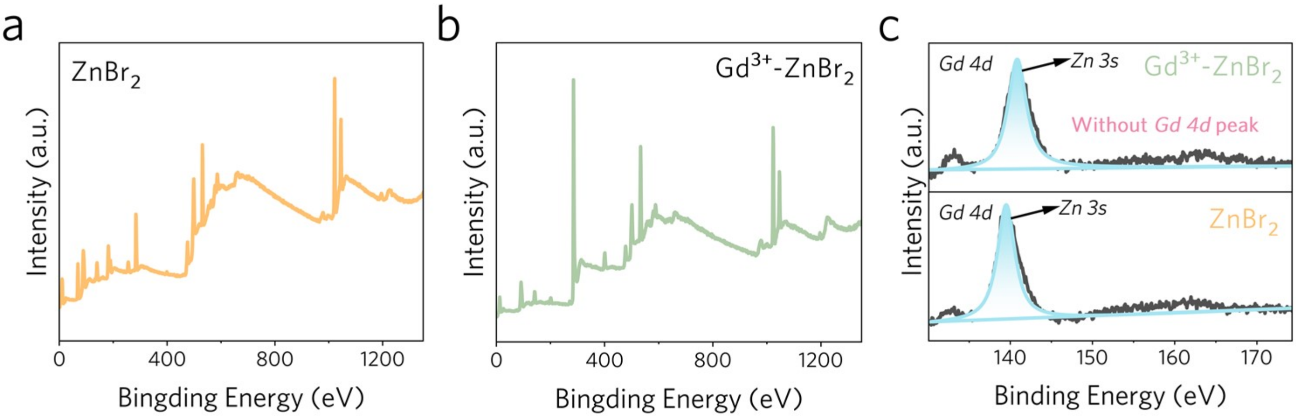

Figure S2. Full XPS spectrums of (a) and (b) carbon felt and the corresponding XPS enlarged spectrum for (c) carbon felts. XPS of Zn crystal growth behavior on CF at 20 mA cm^{-2} in the ZnBr$_2$ and Gd^{3+}-ZnBr$_2$ electrolytes.

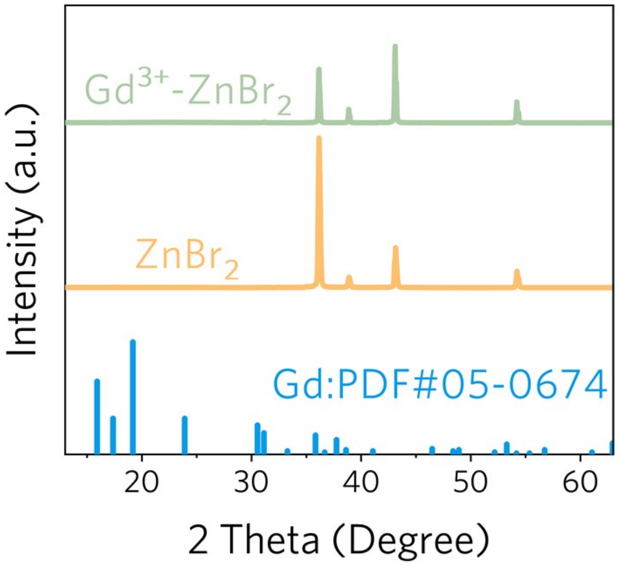

Figure S3. XRD patterns of Zn crystal growth behavior on CF at 20 mA cm^{-2} in the ZnBr$_2$ and Gd^{3+}-ZnBr$_2$ electrolytes, respectively.

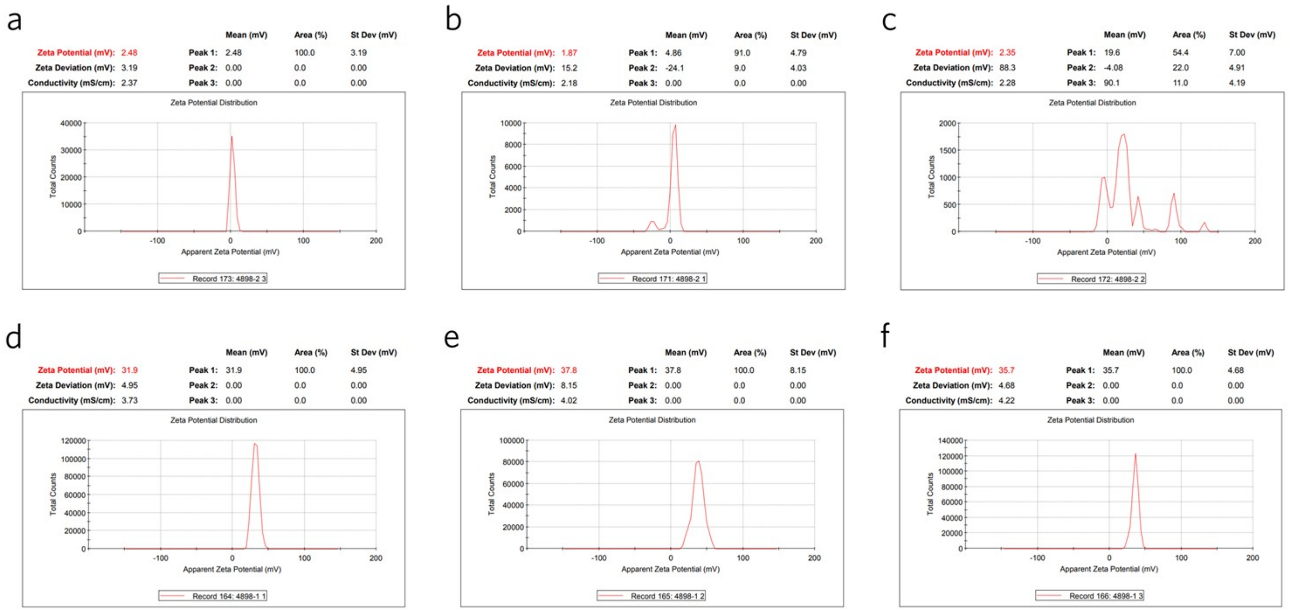

a

Zeta Potential (mV): 2.48
Zeta Deviation (mV): 3.19
Conductivity (mS/cm): 2.37

	Mean (mV)	Area (%)	St Dev (mV)
Peak 1:	2.48	100.0	3.19
Peak 2:	0.00	0.0	0.00
Peak 3:	0.00	0.0	0.00

b

Zeta Potential (mV): 1.87
Zeta Deviation (mV): 15.2
Conductivity (mS/cm): 2.18

	Mean (mV)	Area (%)	St Dev (mV)
Peak 1:	4.86	91.0	4.79
Peak 2:	-24.1	9.0	4.03
Peak 3:	0.00	0.0	0.00

c

Zeta Potential (mV): 2.35
Zeta Deviation (mV): 88.3
Conductivity (mS/cm): 2.28

	Mean (mV)	Area (%)	St Dev (mV)
Peak 1:	19.6	54.4	7.00
Peak 2:	-4.08	22.0	4.91
Peak 3:	90.1	11.0	4.19

d

Zeta Potential (mV): 31.9
Zeta Deviation (mV): 4.95
Conductivity (mS/cm): 3.73

	Mean (mV)	Area (%)	St Dev (mV)
Peak 1:	31.9	100.0	4.95
Peak 2:	0.00	0.0	0.00
Peak 3:	0.00	0.0	0.00

e

Zeta Potential (mV): 37.8
Zeta Deviation (mV): 8.15
Conductivity (mS/cm): 4.02

	Mean (mV)	Area (%)	St Dev (mV)
Peak 1:	37.8	100.0	8.15
Peak 2:	0.00	0.0	0.00
Peak 3:	0.00	0.0	0.00

f

Zeta Potential (mV): 35.7
Zeta Deviation (mV): 4.68
Conductivity (mS/cm): 4.22

	Mean (mV)	Area (%)	St Dev (mV)
Peak 1:	35.7	100.0	4.68
Peak 2:	0.00	0.0	0.00
Peak 3:	0.00	0.0	0.00

Figure S4. Zeta potentials of Zn powder in (a-c) ZnBr$_2$ electrolyte and (d-f) Gd^{3+}-ZnBr$_2$ electrolyte, respectively. Commercial Zn powder is used as a substitute for Zn foil due to the experimental need to disperse Zn in the electrolyte.

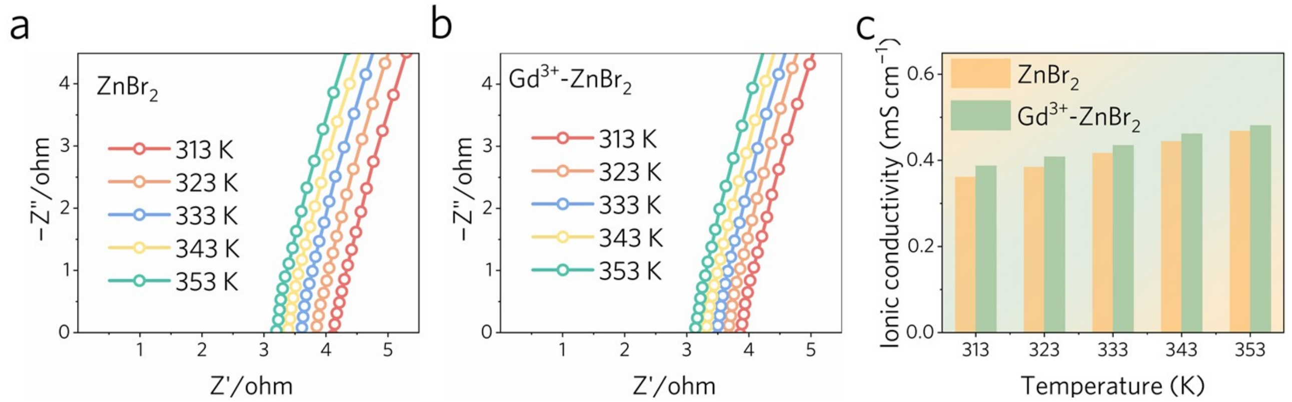

Figure S5. (a) and (b) EIS of Ti||Ti symmetric devices with different electrolytes at different temperatures. (c) The ionic conductivity of the electrolyte is calculated from (a) and (b). The ionic conductivity of the electrolyte is determined through the Equation:

$$\sigma = \frac{L}{R_e \times A}\#(1)$$

Where σ, L, R_e and A represent the ionic conductivity, the distance between the two Ti electrodes, the resistance of the electrolyte, and the cross-sectional area of the electrode, respectively. The R_e is correlated to the EIS (**Figure S5a and 5b**).

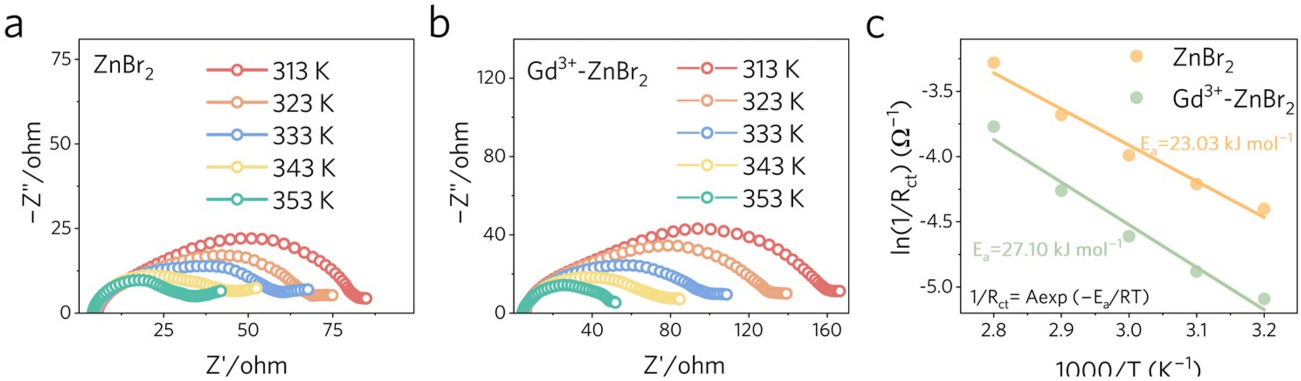

Figure S6. (a) and (b) EIS of Zn||Zn symmetric devices with different electrolytes at different temperatures. (c) Activation energy of the electrolyte is calculated from (a) and (b). The activation energy of the electrolyte is determined through the Equation:

$$\frac{1}{R_{ct}} = Aexp\left(\frac{-E_a}{RT}\right)\#(2)$$

where R_{ct}, A, R, T, and E_a represent the charge transfer resistance, the constant, the gas constant, the Kelvin temperature, and the activation energy, respectively. The R_{ct} is correlated to the semicircles of the EIS profile within the high-frequency range (**Figure S6a and 6b**).

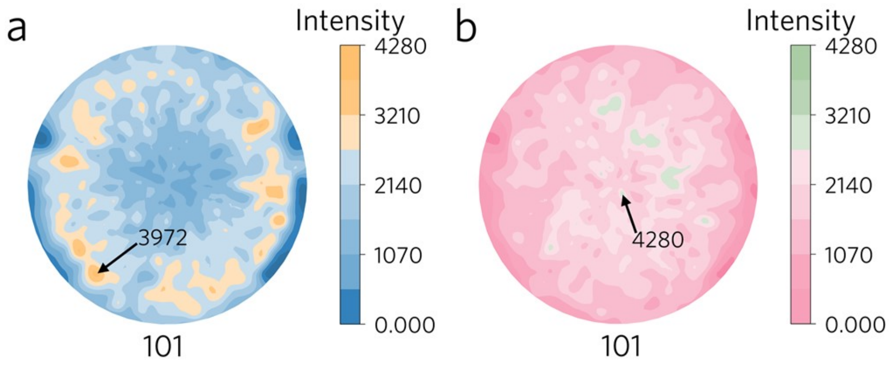

Figure S7. (101) facet pole figures of Zn crystal growth behavior on CF at 20 mA cm^{-2} for 30 minutes in (a) $ZnBr_2$ electrolyte and (b) Gd^{3+}-$ZnBr_2$ electrolyte.

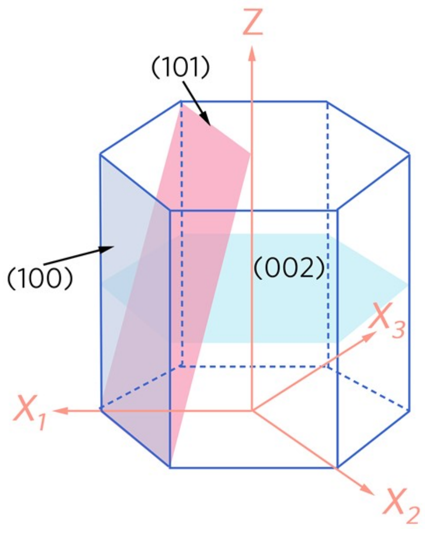

Figure S8. Illustration of the hexagonal close packed (hcp) structure of Zn.

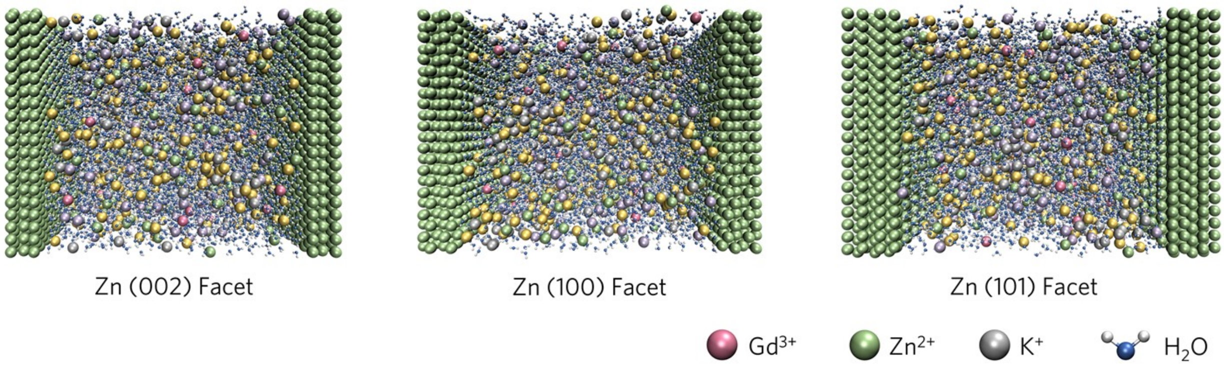

Figure S9. Visual representation and simulation box of Gd^{3+}-$ZnBr_2$ electrolyte species under the constraint of three Zn electrodes with different crystallographic orientations.

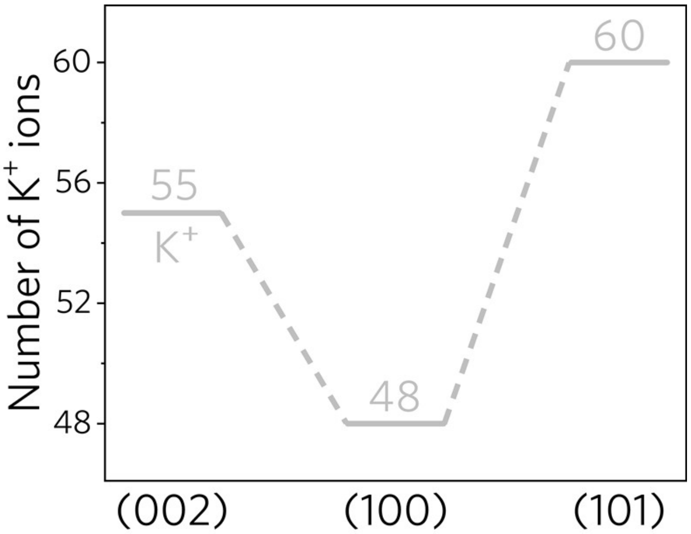

Figure S10. Number of K^+ ions in the Inner Helmholtz Plane (IHP).

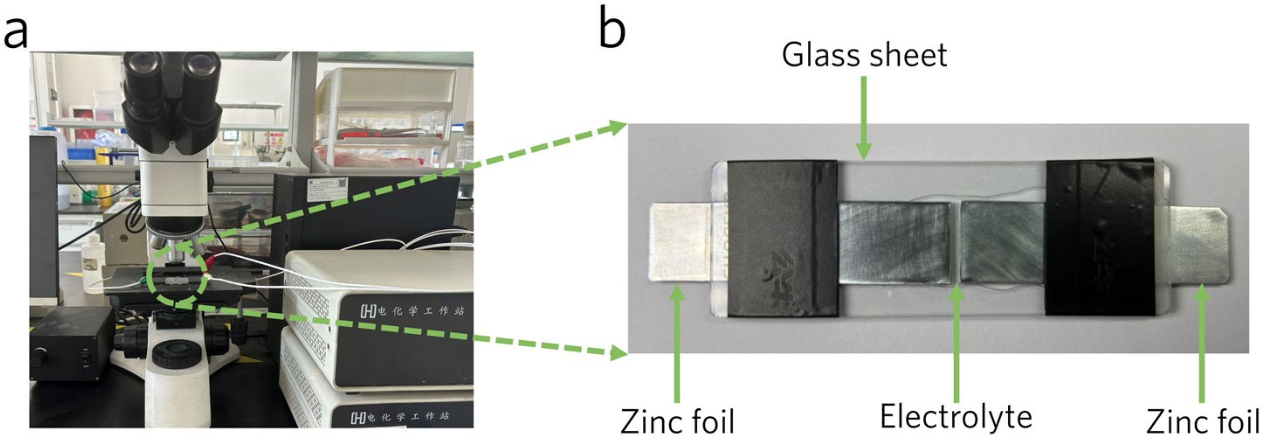

Figure S11. (a) An optical microscope and electrochemical workstation are used for *in situ* optical microscopy testing. (b) Schematic of the materials setup for optical microscopy testing. Zn foils are inserted on both sides of two transparent glass sheets, and the electrolyte is added into the pore between them. During testing, the Zn foils are connected to an electrochemical workstation, and Zn deposition is induced at a constant current. The morphology of the Zn deposition is observed using an optical microscope.

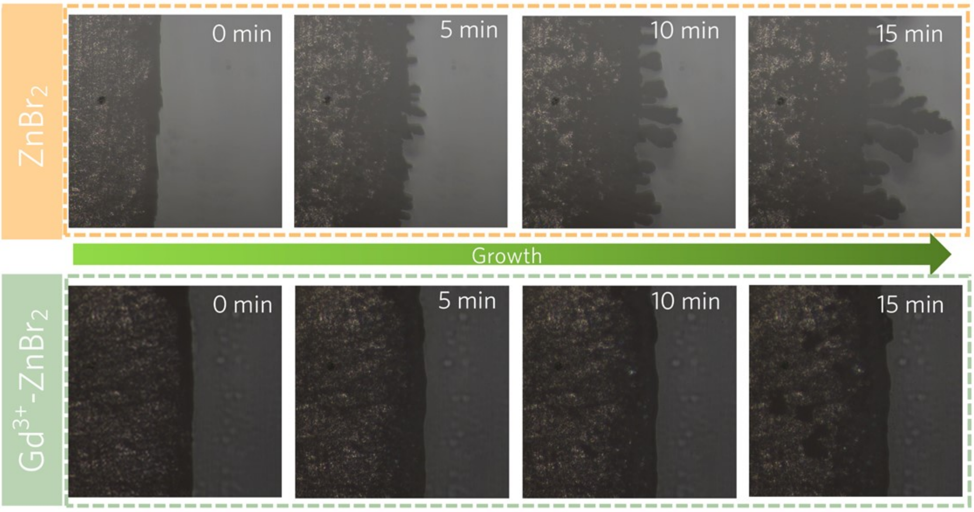

Figure S12. Optical tracking *in situ* of Zn crystal growth behavior in $ZnBr_2$ and Gd^{3+}-$ZnBr_2$ electrolyte systems at 20 mA cm^{-2}.

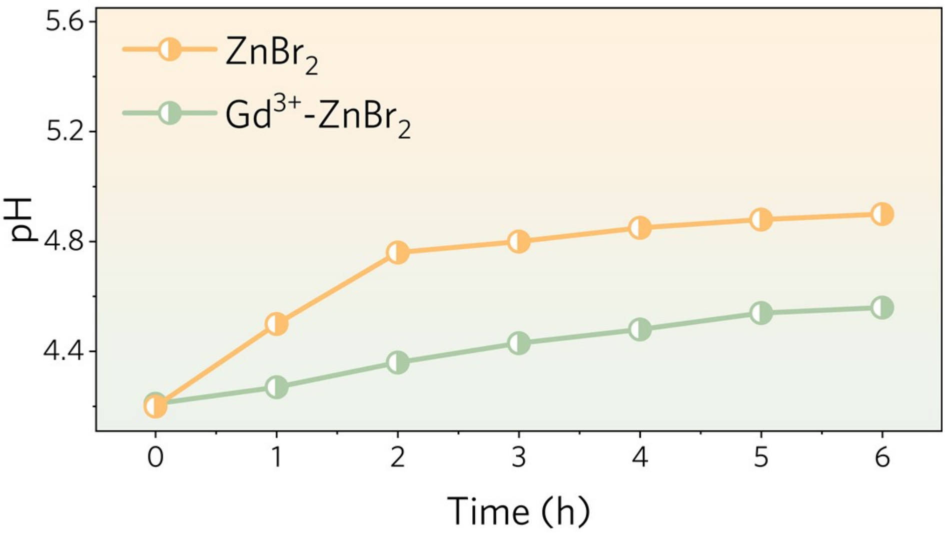

Figure S13. The pH monitoring curves of electrolytes at different times, obtained through *in situ* pH measurements using a pH meter.

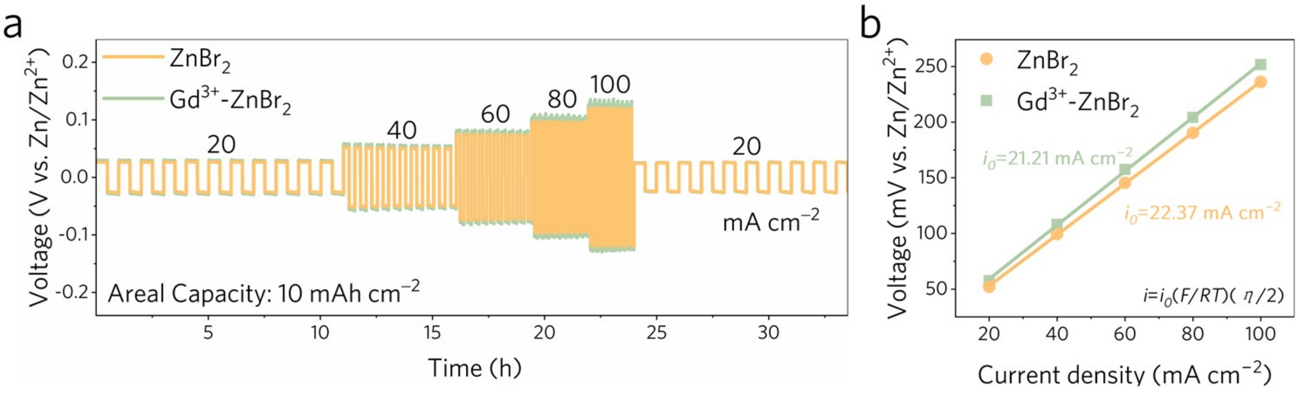

Figure S14. (a) Voltage profiles of Zn||Zn flow batteries utilizing ZnBr$_2$ and Gd^{3+}-ZnBr$_2$ electrolytes at different current densities. (b) Exchange current density in the pure ZnBr$_2$ and Gd^{3+}-ZnBr$_2$ electrolyte. The exchange current density (i_0) is determined from these galvanostatic charge-discharge (GCD) curves. The exchange current density associated with Zn deposition is calculated through the Equation:

$$i = i_0 \frac{\eta F}{2RT} \#(3)$$

where i, i_0, R, T, η, and F represent the current density, exchange current density, gas constant, deposition temperature, voltage hysteresis, and Faraday constant, respectively.

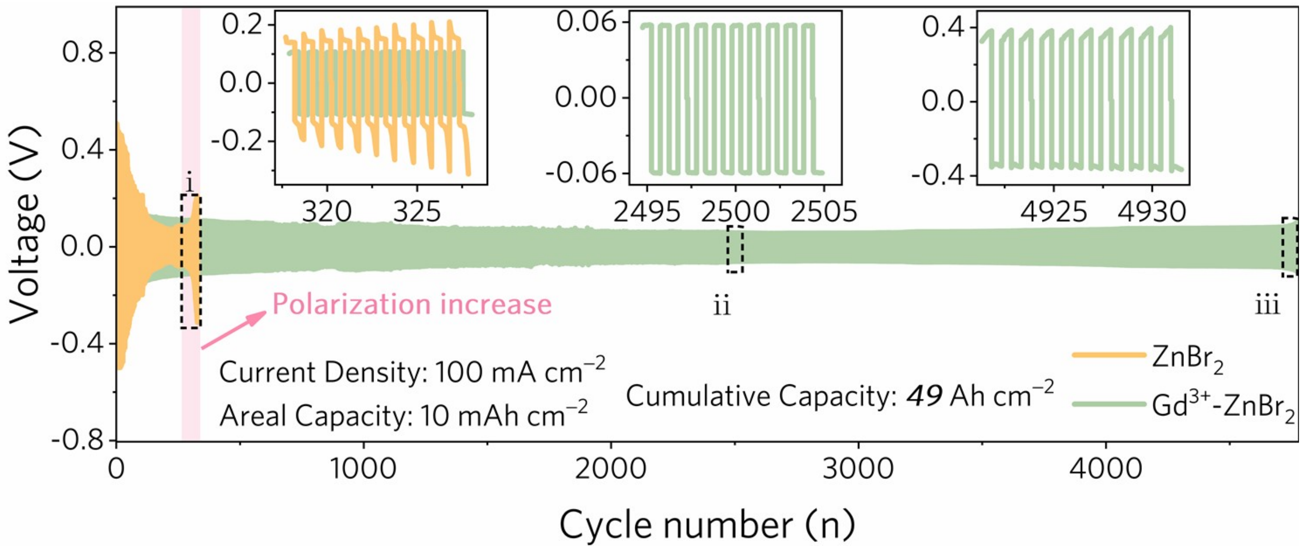

Figure S15. Voltage profiles of Zn||Zn flow batteries utilizing $ZnBr_2$ and Gd^{3+}-$ZnBr_2$ electrolytes at 100 mA cm^{-2} and 10 mhA cm^{-2}, insets show the amplified profile at different cycles.

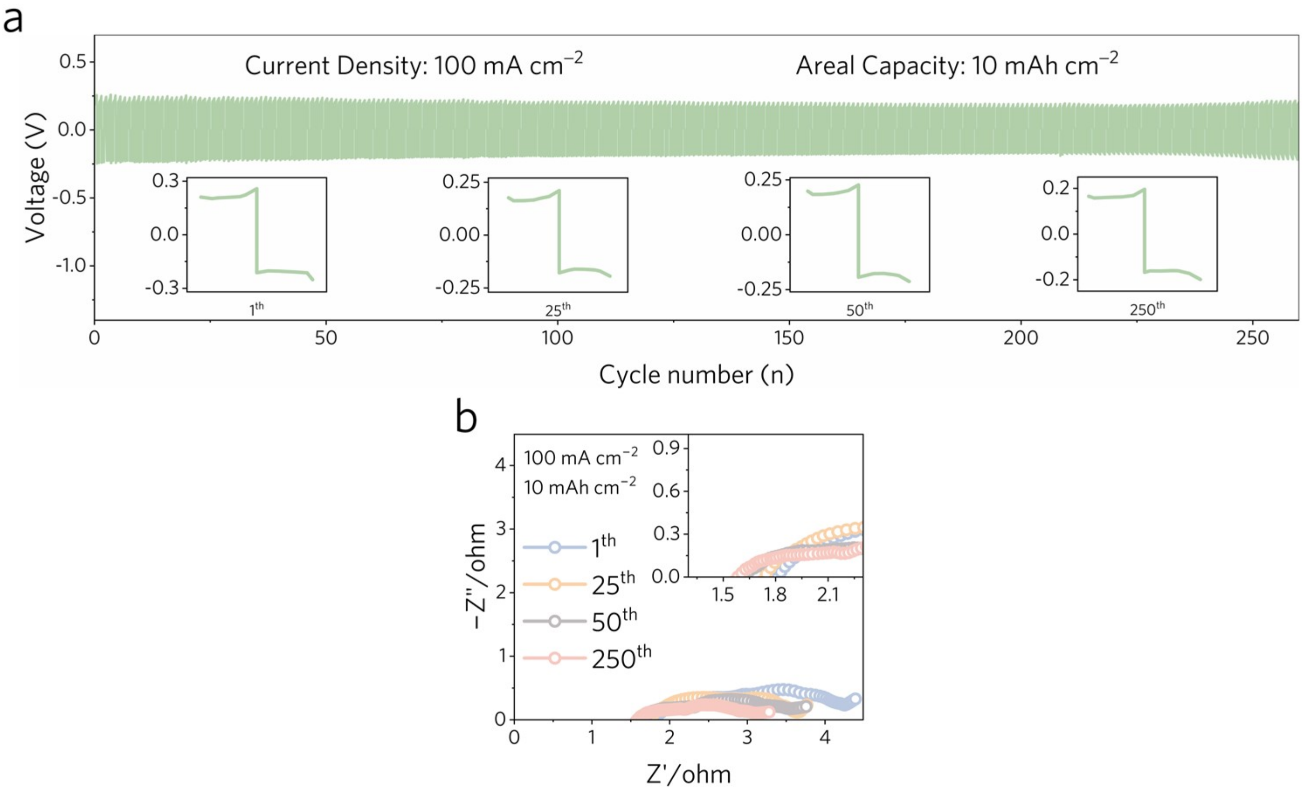

Figure S16. Protocols proposed to detect SS. (a) Voltage profile at 100 mA cm^{-2} and 10 mAh cm^{-2}, with insets showing the amplified profiles at different cycles. (b) Features of symmetric batteries in normal conditions: impedance spectra with different cycles.

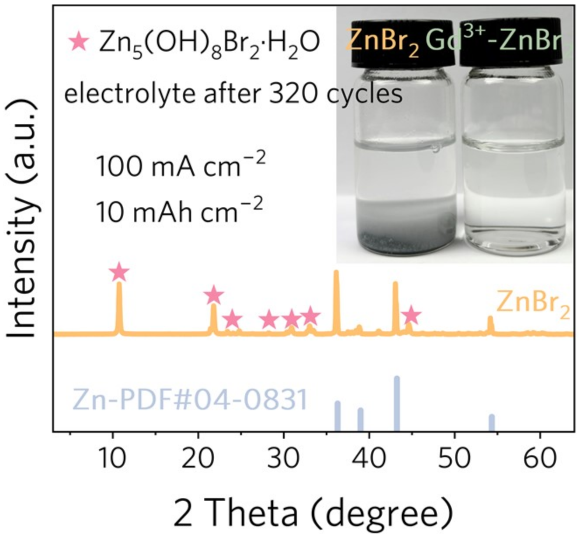

Figure S17. XRD of precipitates in $ZnBr_2$ electrolyte after 320 cycles at 100 mA cm^{-2} and 10 mAh cm^{-2}. The inset shows the XRD of pure $ZnBr_2$ and Gd^{3+}-$ZnBr_2$ electrolytes after 320 cycles.

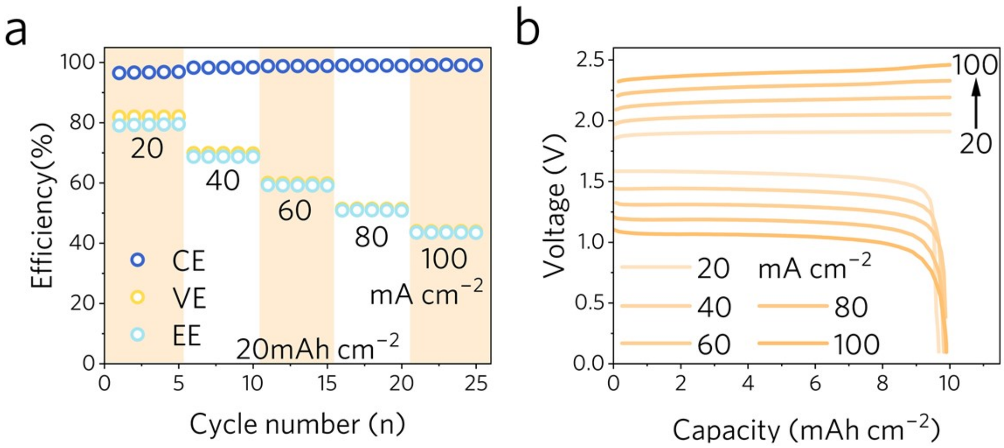

Figure S18. (a) Rate performance of the Zn-Br flow batteries with pure $ZnBr_2$ electrolyte at different current densities. (b) Charge-discharge curves of the Zn-Br flow batteries with pure $ZnBr_2$ electrolyte at different current densities.

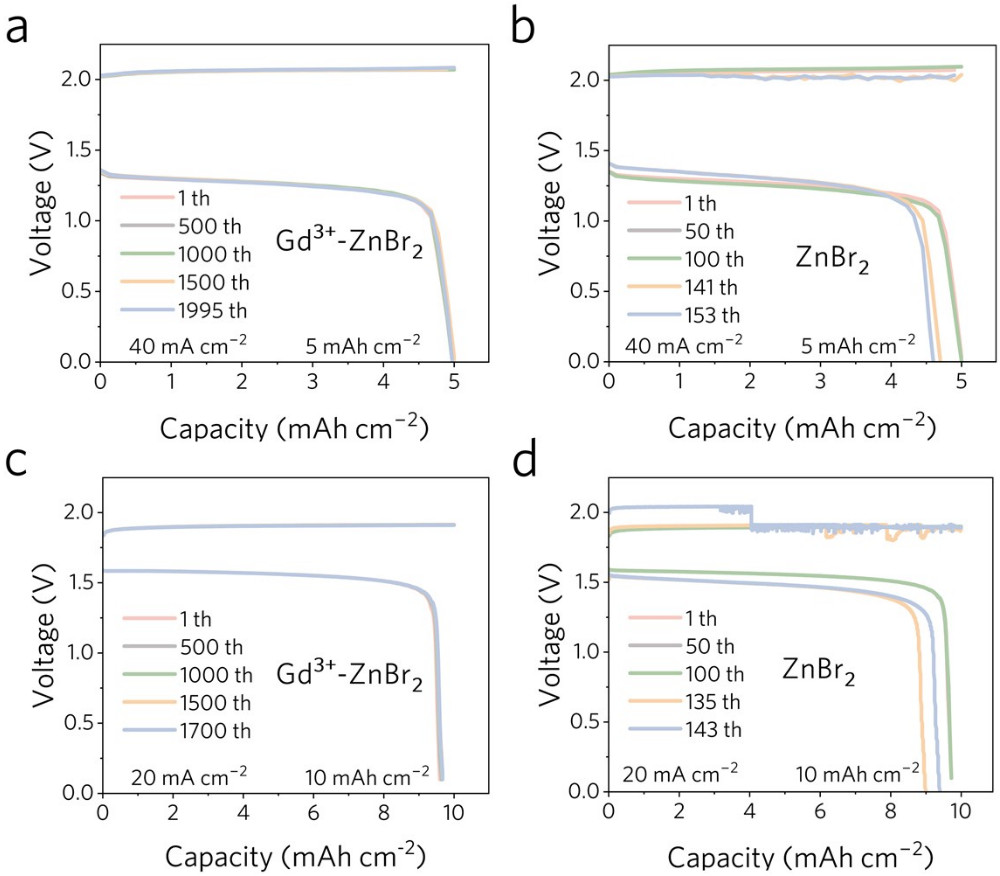

Figure S19. Charge-discharge curves of the Zn-Br flow batteries at (a, b) 40 mA cm^{-2} (5 mAh cm^{-2}) and (c, d) 20 mA cm^{-2} (10 mAh cm^{-2}).

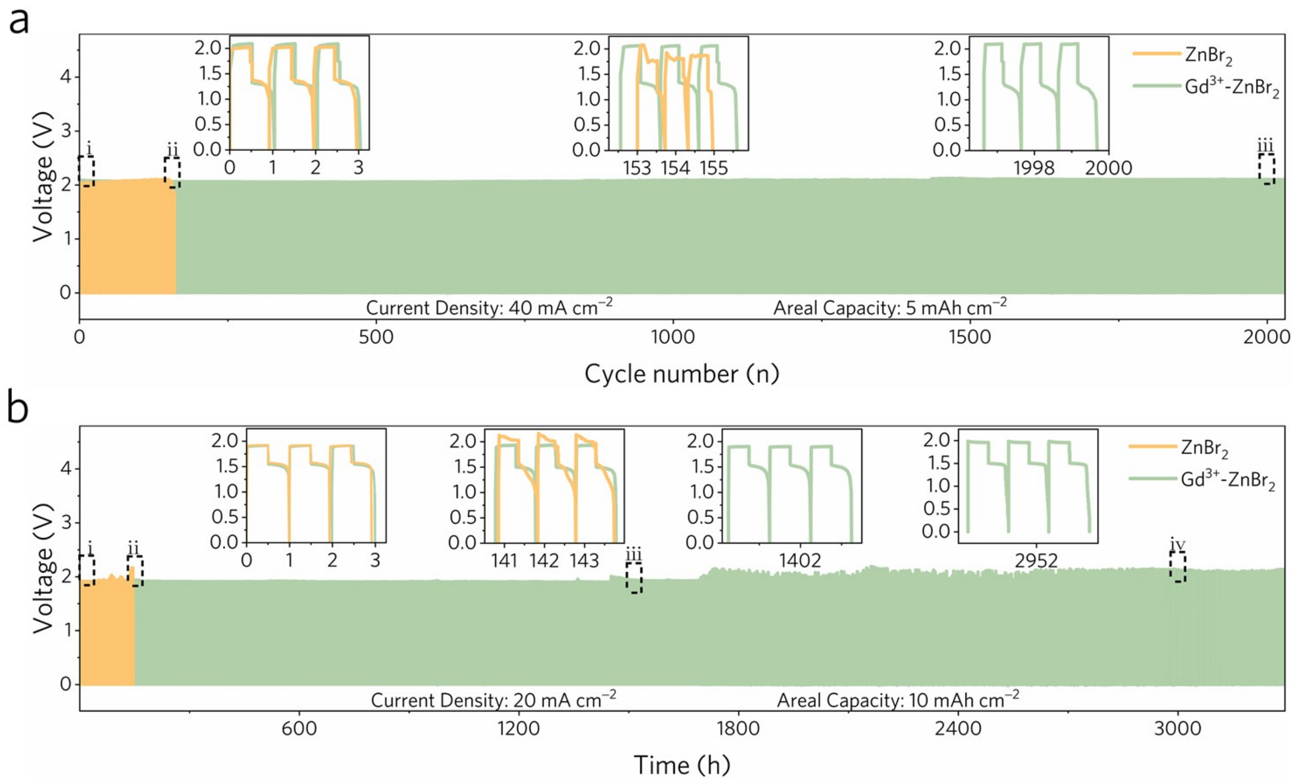

Figure S20. Voltage profile at 40 mA cm^{-2} (5 mAh cm^{-2}) in (a) and 20 mA cm^{-2} (10 mAh cm^{-2}) in (b), insets show the amplified profile at different cycles.

Table S1. Summarization of the intensities of different crystal planes in the experimental sample $I_{(hkl)}$ and standard oriented sample $I_{0(hkl)}$ employing different electrolytes.

	Crystal plane	**(002)**	**(100)**	**(101)**
$ZnBr_2$ electrolyte	I_0	53	40	100
	$I_{2\ min}$	29155	15986	54986
	$I_{5\ min}$	52222	22478	89654
	$I_{10\ min}$	64351	25851	121334
	$I_{20\ min}$	69654	26471	95382
	$I_{30\ min}$	106544	27109	132606
	Crystal plane	**(002)**	**(100)**	**(101)**
Gd^{3+}-$ZnBr_2$ electrolyte	I_0	53	40	100
	$I_{2\ min}$	61526	27978	105252
	$I_{5\ min}$	71173	35483	128583
	$I_{10\ min}$	74541	32687	140799
	$I_{20\ min}$	82845	32024	161704
	$I_{30\ min}$	32173	19185	68501

Table S2. Number of ions and molecules, the total number of atoms, and the size of the simulation box for the modeling system.

	No. of Zn^{2+}	No. of Gd^{3+}	No. of K^+	No. of Cl^-	No. of Br^-	No. of NO_3^-	No. of H_2O	Total no. of atoms	Simulation box size
0.3 M $Gd(NO_3)_3$ 2.5 M KCl 2.0 M $ZnBr_2$	200	30	250	250	400	90	5550	18140	5.1*5.3*5.8 nm^3

Table S3. Numbers of different cations in the Inner Helmholtz Plane (IHP).

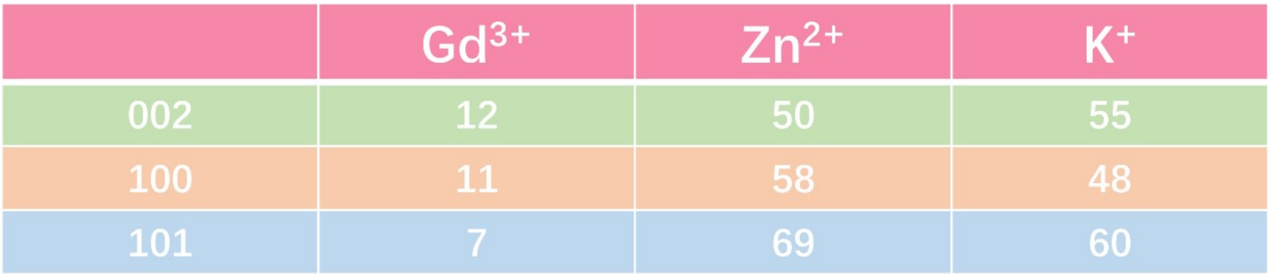

	Gd^{3+}	Zn^{2+}	K^+
002	12	50	55
100	11	58	48
101	7	69	60

Table S4. Current density, energy efficiency, and cumulative capacity with other reported literature evaluate the Zn@CF anode reversibility in ZBFBs. The cumulative capacity is calculated using the following formula:

$$C = n\int_{0}^{t} \frac{i\,dt}{A} \#(4)$$

where *n* is number of cycles, *A* is reaction area, *i* is the current.

Reference No.	Current density (mA cm^{-2})	Coulombic efficiency (%)	Cumulative capacity (Ah cm^{-2})	Cycle number (n)
This work	**20**	**98**	**33.25**	**3300**
	40	**99.61**	**10**	**2000**
1	10	95.6	9.72	400
2	20	95	3.334	200
3	20	98.25	2	200
4	20	95.39	8	100
5	20	95	1	100
6	40	99.88	3	150
7	40	91.3	3.47	45
8	40	98.94	10	500
9	80	99.5	4	400
10	80	96.6	4	200

Reference

1 Hee Han, S.; Kim, S.; Yong Lim, H.; Park, S.; Shin, K.; Kim, S.; Kim, H.-T.; Kyu Kwak, S.; Yang, C.; Choi, N.-S. Modified viologen-assisted reversible bromine capture and release in flowless zinc–bromine batteries. ***Chemical Engineering Journal*** 2023, 464.

2 Chenhui Wang, Xianfeng Li, Xiaoli Xi, Pengcheng Xu, Qinzhi Lai & Huamin Zhang. Relationship between activity and structure of carbon materials for Br_2/Br^- in zinc bromine flow batteries. ***RSC Advances***, 2016, 46, 40169-40174.

3 Lee Y, Yun D, Park J, et al. An organic imidazolium derivative additive inducing fast and highly reversible redox reactions in zinc-bromine flow batteries[J]. ***Journal of Power Sources***, 2022.

4 Wang, S.; Wang, Z.; Yin, Y.; Li, T.; Chang, N.; Fan, F.; Zhang, H.; Li, X. A highly reversible zinc deposition for flow batteries regulated by critical concentration induced nucleation. ***Energy & Environmental Science*** 2021, 14 (7), 4077-4084.

5 Suresh S, Ulaganathan M, Pitchai R. Realizing highly efficient energy retention of Zn–Br_2 redox flow battery using rGO supported 3D carbon network as a superior electrode[J]. ***Journal of Power Sources***, 2019, 438:226998.

6 Kim, M.; Yun, D.; Jeon, J. Effect of a bromine complex agent on electrochemical performances of zinc electrodeposition and electrodissolution in Zinc–Bromide flow battery. ***Journal of Power Sources*** **2019**, *438*.

7 Bae, S.; Lee, J.; Kim, D. S. The effect of Cr^{3+}-Functionalized additive in zinc-bromine flow battery. ***Journal of Power Sources*** **2019**, *413*, 167-173.

8 Gikunoo, E. K.; Han, D.; Vinothkannan, M.; Shanmugam, S. Synthesis and characterization of highly durable hydrocarbon-based composite membrane for zinc-bromine redox flow battery. ***Journal of Power Sources*** 2023, 563.

9 Li Y, Li L, Xu W, et al. Promoted efficiency of zinc bromine flow batteries with catalytic Co-N-C composite cathode[J]. ***Journal of Power Sources***, 2024, 599: 234208.

10 Wang, C.; Li, X.; Xi, X.; Zhou, W.; Lai, Q.; Zhang, H. Bimodal highly ordered mesostructure carbon with high activity for Br_2/Br^- redox couple in bromine based batteries. ***Nano Energy*** 2016, 21, 217-227.